JOURNAL OF COMPUTATIONAL PHYSICS 120, 48–65 (1995)

Gas-Kinetic Finite Volume Methods, Flux-Vector Splitting, and Artificial Diffusion

KUN XU, LUIGI MARTINELLI, AND ANTONY JAMESON

Department of Mechanical and Aerospace Engineering, Princeton University, Princeton, New Jersey 08544

Received July 13, 1994

In order to improve our understanding of Boltzmann-type schemes, which have been recently proposed for the Euler and Navier–Stokes equations by Prendergast and Xu, we have modified the gas-kinetic approach and applied it to simple hyperbolic conservation laws. We found that the gas-kinetic discretization can be explained in terms of standard central difference and upwind schemes. Artificial viscosity concepts are reviewed and linked to the grid size and the physical length scale of the discontinuity. Also, a new three-dimensional gas-kinetic scheme for the numerical Navier–Stokes equations, whose solution satisfies the entropy condition, is presented. Two numerical limits of the scheme are obtained. The first one is the one-step Lax–Wendroff scheme, and the second one is the kinetic flux vector splitting scheme. A new relaxation scheme for steady state calculations is also formulated and implemented in the multigrid time stepping technique of Jameson. When applied to the Euler equations, the resulting method yields high accuracy and fast convergence to a steady state.

1. INTRODUCTION

Many high resolution shock capturing schemes have been developed in the past 15 years. Most of them either attempt to resolve wave interactions through upwind biasing of the discretization, or else explicitly introduce numerical viscosity in just the amount needed to resolve discontinuities which result from wave interactions. Since many standard upwind schemes can be recovered exactly by the addition of appropriately defined numerical viscosity to a central difference scheme, the two class of schemes are not entirely different, and a unified theory covering both approaches can be developed [13, 20, 40].

High-order upwind schemes are closely related to the propagation of characteristics. Well-known examples are flux vector splitting and Godunov-type schemes. The interpolation techniques first create discontinuities at cell boundaries, and the wave interactions formed from these discontinuities are followed. A high-resolution interpolation in space will not produce a final scheme with the same order of accuracy in time if the Riemann problem is simply solved according to the initial "jump." The temporal accuracy of upwind schemes can be improved either by implementing a Runge–Kutta integration method [38] or by capturing complicated wave interactions inside a time step [2, 6, 11]. In an upwind scheme, physical discontinuities are usually captured accurately by the inclusion of implicit viscosity built into the scheme. However, an entropy fix, in which viscosity is explitiely added in the neighborhood of the sonic point, is generally needed to prevent unphysical discontinuous expansions.

When numerical viscosity is added explicitly, the starting point is usually a central difference formula, the construction of which implicitly assumes a continuous distribution of the physical quantities. This assumption is intrinsically correct in smooth regions. Second-order temporal accuracy can be achieved with the Lax–Wendroff technique. To avoid the cost of calculating the Jacobian matrices connecting the spatial and temporal terms either predictor–corrector or Runge–Kutta methods are often preferred [16, 22]. Discontinuities invalidate, however, the basic assumption behind a central difference scheme. So do thin shocks or shear layers in viscous solutions, when the layer thickness is much smaller than the cell size of the mesh. Artificial viscosity is therefore introduced to suppress the oscillations which would otherwise appear. Its role is quite similar to that of physical viscosity, in that it produces a discontinuous layer of finite thickness, which needs to be of the same order of the cell size to allow for proper resolution on the computational mesh. The required coefficient of numerical viscosity is at least equal to one-half the product of the wave speed and the cell width. The use of the minimum coefficient recovers the first-order upwind scheme [18, 20]. The connection between upwinding and artificial viscosity was already recognized in the study of transonic potential flow [14, 15]. When it is introduced in the proper amount, numerical viscosity also assures that the solution will satisfy the entropy condition [1]. In this crucial role it again has an effect similar to that of the true viscosity.

Some viscosity is also needed in smooth regions to prevent odd–even decoupling. In order to obtain higher order accuracy, it is necessary either to switch to a higher order diffusive flux, or else to compensate the diffusion by controlled anti-diffusive terms. Recently, Jameson has derived a new family of artificial diffusion models based on the local extremum diminishing (LED) principle [20]. The essential requirements of a good numerical scheme are high accuracy in the treatment of continu-

0021-9991/95 $12.00

ous flows, especially for Navier–Stokes calculations [42], together with high resolution and clean capture of discontinuous layers. In effect such a scheme should combine the best features of both central difference and upwind approximations.

Due to the intrinsic upwinding and multidimensional properties of particle motion, gas-kinetic schemes [12, 35] have begun to attract increasing attention. Chu [5], Sanders and Prendergast [37], Pullin [30], Reitz [32], Macrossan [24], Desphande [8], Perthame [27], Eppard and Grossman [10] and many others have investigated and constructed this kind of schemes. Most of the schemes developed so far are based on the collisionless Boltzmann equation, yielding results which are more diffusive than those obtained from classical high resolution difference schemes. In order to overcome this problem, a new gas-kinetic method based on the collisional BGK model has been developed for both the Euler and Navier–Stokes equations [29, 47]. In this paper, we modify the original method and study its connections with the Lax–Wendroff and flux–vector splitting schemes.

This paper is organized as follows. Section 2 describes the application of the general gas-kinetic technique to the linear advection equation. Section 3 presents a new scheme for the 3D Navier–Stokes solutions, followed by some important analysis, such as the entropy condition. Also, a simplified gas-kinetic relaxation scheme for the steady state Euler equations is derived at the end of this section. Section 4 is about the numerical examples for both steady and unsteady flow calculations. Finally, some concluding remarks will be presented.

2. GAS-KINETIC DESCRIPTION OF HYPERBOLIC CONSERVATION LAW

Perthame and Tadmor [28] have proved that a nonlinear kinetic equation is well suited to describe general multidimensional scalar conservation laws. The gas kinetic construction for hyperbolic equations, is however, not unique. In this section, we present a specific gas-kinetic construction for the linear advection equation. The resulting equation is solved numerically by applying the techniques developed in [29, 47]. At the same time, some modifications of the original schemes are presented. At the end of this section we analyze the resulting numerical flux, and contrast them with classical Lax–Wendroff and upwind methods.

2.1. *Gas-Kinetic Reconstruction of the Linear Advection Equation*

Roe pointed out that most upwind schemes essentially describe a mechanism by which any algorithm developed for the numerical solution of the linear advection equation $U_t + cU_x = 0$ can be generalized to the case of the non-linear system [35]. Gas-kinetic schemes based on the Boltzmann equation are formulated instead directly for the Euler and Navier–Stokes equations. This complicates the analysis for the simple linear problem since a gas-kinetic description for the linear advection equation must be constructed first.

Consider the linear advection equation

$$U_t + cU_x = 0, \tag{1}$$

where U is the solution and c is the wave speed. For any numerical scheme, the smallest length scale that can be resolved is the grid size Δx. In reality, a sharp gradient or discontinuity could exist with the length scale δl such that $\delta l \ll \Delta x$. Since the numerical grid size Δx requires us to approximate $\delta l \simeq \Delta x$ at best, we must increase artificially the thickness of discontinuities. As a result, the real equation to be solved is $U_t + cU_x = \nu U_{xx}$, rather than Eq. (1), where ν makes $\delta l \simeq \Delta x$ near discontinuities, and it should be reduced as much as possible in smooth regions.

In order to approach Eq. (1) from gas-kinetics, U must be considered as an average quantity of a group of microscopic particles. The dynamics of these particles can be described by a distribution function $f(x, t, u)$, defined as

$$U(x, t) = \int_{-\infty}^{+\infty} f(x, t, u)\, du,$$

where u is the individual particle velocity. The evolution of f is properly described by the Boltzmann equation, where bimolecule collisions are considered. However, due to the intrinsic difficulty of solving the collisional term in the Boltzmann equation, approximate collisional models are usually used. One of the widely used models is the BGK model [3]. This is

$$f_t + uf_x = (g - f)/\tau, \tag{2}$$

where g is the equilibrium state which the real gas distribution function f approaches in a time scale of the order of the collision time τ which is a local constant. Since the integrals of g and f in velocity space represent the same macroscopic quantity U, we have the following compatibility relation

$$\int_{-\infty}^{+\infty} (f - g)\, du = 0 \quad \forall x, t. \tag{3}$$

For the linear advection equation, the equilibrium state g can be constructed as

$$g = \sqrt{\lambda/\pi}\, U e^{-\lambda(u-c)^2},$$

where U and c are the corresponding quantities in Eq. (1), and $1/\lambda$ is an equivalent temperature. In an equilibrium state, when $f = g$, Eq. (2) reduces to $g_t + ug_x = 0$, which allows the precise recovery of the linear advection (Eq. (1)) through integration

in velocity space,

$$\frac{\partial}{\partial t}\int_{-\infty}^{+\infty} g\,du + \frac{\partial}{\partial x}\int_{-\infty}^{+\infty} ug\,du = 0.$$

On the other hand, by using a Chapman–Enskog expansion, one obtains the viscous advection equation

$$U_t + cU_x = \nu U_{xx} \tag{4}$$

directly from Eq. (2). Here, the viscosity coefficient ν depends on the gas temperature $1/\lambda$ and collision time τ through the relation

$$\nu = \frac{\tau}{2\lambda}.$$

Therefore, a numerical scheme developed from Eq. (2) will automatically be suitable for Eq. (4), and the viscosity coefficient ν can be controlled through the collision time and gas temperature.

2.2. *Gas-Kinetic Scheme for the Advection Equation*

The numerical flux is the moment of the gas distribution function f, defined by

$$\mathcal{F}(x,t) = \int_{-\infty}^{\infty} uf(x,t,u)\,du.$$

In the one-dimensional case, by letting x_j be the cell center and $x_{j+1/2}$ the cell interface, Eq. (2) can be integrated over u, x, and t, to yield the update formula

$$U_j^{n+1} = U_j^n + \int_{t^n}^{t^{n+1}} (\mathcal{F}(x_{j-1/2},t) - \mathcal{F}(x_{j+1/2},t))\,dt,$$

where n is the step number and $T = t^{n+1} - t^n$ is the time step. In the following, without loss of generality, the initial time t^n will be assumed to be zero.

To complete the numerical scheme f must be estimated at cell boundaries. The general solution of f from Eq. (2) at the cell interface $x_{j+1/2}$ is

$$f(x_{j+1/2},t,u) = \frac{1}{\tau}\int_0^t g(x',t',u)e^{-(t-t')/\tau}\,dt' + e^{-t/\tau}f_0(x_{j+1/2} - ut), \tag{5}$$

where $x' = x_{j+1/2} - u(t - t')$ is the particle's trajectory, and f_0 is the initial gas distribution function f at time $t = 0$. This solution requires explicit expressions for both the equilibrium state g and the initial nonequilibrium gas distribution function f_0. In order to simplify the notation and without loss of generality, we derive the formulas at the cell boundary $x_{j+1/2} = 0$ using a cell size $\Delta x = 1$.

In smooth regions, it is reasonable to assume that the initial gas distribution function f_0 is a Maxwellian around $x = 0$. However, near discontinuities, two different distribution functions to the left and right sides of the cell boundary should be assumed, especially in the case where the cell size is much larger than the discontinuity thickness. Thus, we can expand $f_0(x)$ separately on both sides of the cell boundary. To second-order accuracy, f_0 can be taken as

$$f_0(x) = \begin{cases} g^l(1 + a^l x), & x < 0 \\ g^r(1 + a^r x), & x > 0 \end{cases} \tag{6}$$

where both $g^l = \sqrt{\lambda/\pi}\,\overline{U}_l e^{-\lambda(u-c)^2}$ and $g^r = \sqrt{\lambda/\pi}\,\overline{U}_r e^{-\lambda(u-c)^2}$ are Maxwellians, and a^l and a^r are local constants, respectively to the left and to the right of the cell interface. There are four unknowns $\overline{U}_l$, a^l, $\overline{U}_r$, and a^r, which must be found from the initial data U_j at $t = 0$. As with the Godunov-type schemes, a variety of interpolation techniques can be used here. For example, $\overline{U}_l = U_j$, $a^l = 0$, $\overline{U}_r = U_{j+1}$, and $a^r = 0$ yield a first-order accurate scheme.

Jameson has recently developed a general symmetric limited positive (SLIP) formulation from the local extremum diminishing (LED) principle [20]. Following the SLIP construction, a^l, a^r, $\overline{U}_l$, and $\overline{U}_r$ can be expressed as

$$\begin{aligned} \overline{U}_l &= U_j + \tfrac{1}{2}e_j \\ \overline{U}_r &= U_{j+1} - \tfrac{1}{2}e_{j+1} \\ a^l &= \frac{e_j}{\overline{U}_l} \\ a^r &= \frac{e_{j+1}}{\overline{U}_r}, \end{aligned} \tag{7}$$

where e_j is the limited average of $e_j = L(\Delta U_{j+1/2}, \Delta U_{j-1/2})$ with $\Delta U_{j+1/2} = U_{j+1} - U_j$, and $L(u, v)$ is a limiter with the following properties:

P_1: $L(u, v) = L(v, u)$

P_2: $L(\alpha u, \alpha v) = \alpha L(u, v)$

P_3: $L(u, u) = u$

P_4: $L(u, v) = 0$ if u and v have opposite sign.

A number of specific limiters L can be found in [41, 20].

The distribution function g corresponding to the equilibrium state will be smoother than f. Thus it can be expanded locally across the cell boundary as

$$g(x,t) = g_0(1 + \bar{a}x + \bar{A}t), \tag{8}$$

where g_0 is a local Maxwellian $g_0 = \sqrt{\lambda/\pi}\,\overline{U}e^{-\lambda(u-c)^2}$, and $\bar{a}$ and $\bar{A}$ are local constants. After taking the limit of Eq. (5) as $t \to 0$ and substituting it into Eq. (3), g_0 at $x = 0$ and $t = 0$

can be obtained from f_0, which is

$$\int_{-\infty}^{+\infty} g_0\,du = \int_{-\infty}^{+\infty} f_0\,du,$$

where

$$f_0 = \begin{cases} g^l, & u > 0, \\ g^r, & u < 0. \end{cases} \tag{9}$$

Hence, $\overline{U}$ can be obtained explicitly as

$$\overline{U} = \tfrac{1}{2}\overline{U}_l \operatorname{erfc}(-\sqrt{\lambda}c) + \tfrac{1}{2}\overline{U}_r \operatorname{erfc}(\sqrt{\lambda}c) \tag{10}$$

where (erfc) is the complementary error function. The other term in Eq. (8), $\bar{a}$, can be obtained at time $t = 0$ from a limited average of the slopes $U_{j+3/2} = U_{j+2} - U_{j+1}$ and $U_{j-1/2} = U_j - U_{j-1}$, as

$$\bar{a} = \frac{e_{j+1/2}}{\overline{U}}, \tag{11}$$

where $e_{j+1/2} = L(\Delta U_{j+3/2}, \Delta U_{j-1/2})$. Now the only unknown term left in Eq. (8) is $\overline{A}$, which must be determined considering the gas evolution. This reconstruction of g_0 differs from that used in previous work of the first author [29, 47], in which $\overline{U}$ was found by simple interpolation of the macroscopic solution U_j. The new formulation introduces an upwind bias which takes into account the motion of individual particles. Although both g and f_0 have been expressed in terms of the equilibrium Maxwellian distributions, they represent different physical quantities: g is the presumed equilibrium state across the cell boundary and f_0 is the initial nonequilibrium gas distribution, which would approach g in the gas evolution process. The nonequilibrium character of f_0, which is made up of two half-Maxwellians, can be inferred from Eq. (9).

Substituting Eq. (6) and Eq. (8) into Eq. (5), one obtains

$$\begin{aligned} f(0, t, u) = {} & (1 - e^{-t/\tau})g_0 + (\tau(-1 + e^{-t/\tau}) + te^{-t/\tau})u\bar{a}g_0 \\ & + \tau(t/\tau - 1 + e^{-t/\tau})\overline{A}g_0 + e^{-t/\tau}f_0(-ut), \end{aligned} \tag{12}$$

which is the desired approximation to the distribution function f at the cell boundary $x_{j+1/2}$. Also, from Eq. (6) we obtain

$$f_0(-ut) = \begin{cases} g^l(1 - a^l ut), & u > 0, \\ g^r(1 - a^r ut), & u < 0, \end{cases}$$

where $\overline{A}$ is the only remaining unknown. The calculation of $\overline{A}$ requires the use of the compatibility constraint equation (3). Combining f and g which are solutions of Eq. (12) and Eq. (8), respectively, we get

$$\begin{aligned} f - g = {} & -e^{-t/\tau}g_0 + (\tau(-1 + e^{-t/\tau}) + te^{-t/\tau})uag_0 \\ & + \tau(-1 + e^{-t/\tau})\overline{A}g_0 + e^{-t/\tau}f_0(-ut). \end{aligned}$$

Substituting the above expression into Eq. (3) and integrating over a whole time step T, we obtain $\overline{A}$ explicitly as

$$\begin{aligned} \overline{A} = {} & \beta_1 + \beta_2 c\bar{a} + \tfrac{1}{2}\beta_3\left\{\frac{\overline{U}_l}{\overline{U}}\operatorname{erfc}(-\sqrt{\lambda}c) + \frac{\overline{U}_r}{\overline{U}}\operatorname{erfc}(\sqrt{\lambda}c)\right\} \\ & + \tfrac{1}{2}\beta_4\left\{\frac{\overline{U}_l a^l}{\overline{U}}\left(\operatorname{erfc}(-\sqrt{\lambda}c)c + \frac{e^{-\lambda c^2}}{\sqrt{\pi\lambda}}\right)\right. \\ & \left. + \frac{\overline{U}_r a^r}{\overline{U}}\left(\operatorname{erfc}(\sqrt{\lambda}c)c - \frac{e^{-\lambda c^2}}{\sqrt{\pi\lambda}}\right)\right\}, \end{aligned}$$

where

$$\begin{aligned} \beta_0 &= T - \tau(1 - e^{-T/\tau}) \\ \beta_1 &= -(1 - e^{-T/\tau})/\beta_0 \\ \beta_2 &= (-T + 2\tau - (2\tau + T)e^{-T/\tau})/\beta_0 \\ \beta_3 &= (1 - e^{-T/\tau})/\beta_0 \\ \beta_4 &= (-\tau + (\tau + T)e^{-T/\tau})/\beta_0. \end{aligned}$$

Note that $(f - g)$ is a function of time and thus the integration over a time step allows the compatibility condition equation (3) to be satisfied on the average. Our procedure for computing f and g removes the stiffness from the original BGK model and allows the determination of the time step T by the usual *macroscopic* Courant–Friedrichs–Lewy (CFL) condition. This will be referred to as the CFL time step in the following paragraphs. Otherwise, the numerical stability condition for Eq. (2) would require $T \leq \tau$, which, as in most lattice gas Boltzmann codes, would strongly restrict the efficiency and applicability of the numerical schemes for hydrodynamic simulations.

Having obtained a complete estimate of the distribution function f at the cell interface, we can write down the final expression for the time dependent numerical flux. From Eq. (12) we obtain

$$\begin{aligned} \mathcal{F}(x_{j+1/2}, t) = {} & (\alpha_1 + \alpha_3\beta_1)c\overline{U} \\ & + \left(\alpha_2\left(c^2 + \frac{1}{2\lambda}\right) + \alpha_3\beta_2 c^2\right)\bar{a}\overline{U} \\ & + \left\{\frac{c}{2}(\alpha_3\beta_3 + \alpha_4)\operatorname{erfc}(-\sqrt{\lambda}c) + \frac{\alpha_4}{2\sqrt{\pi\lambda}}e^{-\lambda c^2}\right\}\overline{U}_l \\ & + \left\{\frac{c}{2}(\alpha_3\beta_3 + \alpha_4)\operatorname{erfc}(\sqrt{\lambda}c) - \frac{\alpha_4}{2\sqrt{\pi\lambda}}e^{-\lambda c^2}\right\}\overline{U}_r \\ & + \left\{\tfrac{1}{2}\left(c^2\alpha_3\beta_4 + \alpha_5\left(c^2 + \frac{1}{2\lambda}\right)\right)\operatorname{erfc}(-\sqrt{\lambda}c)\right. \\ & \left. + \frac{c}{2\sqrt{\pi\lambda}}(\alpha_3\beta_4 + \alpha_5)e^{-\lambda c^2}\right\}a^l\overline{U}_l \end{aligned}$$

$$+\left\{\tfrac{1}{2}\left(c^2\alpha_3\beta_4+\alpha_5\left(c^2+\frac{1}{2\lambda}\right)\right)\operatorname{erfc}(\sqrt{\lambda}c)-\frac{c}{2\sqrt{\pi\lambda}}(\alpha_3\beta_4+\alpha_5)e^{-\lambda c^2}\right\}a^r\overline{U}_r \tag{13}$$

with

$$\alpha_1=(1-e^{-t/\tau}),$$
$$\alpha_2=(\tau(-1+e^{-t/\tau})+te^{-t/\tau})$$
$$\alpha_3=\tau(t/\tau-1+e^{-t/\tau}),$$
$$\alpha_4=e^{-t/\tau},$$
$$\alpha_5=-te^{-t/\tau}.$$

The numerical flux is exact for a uniform flow ($\overline{U}=\overline{U}_l=\overline{U}_r=U$ and $\bar{a}=a^l=a^r=0$), and therefore it satisfies the consistency condition $\mathcal{F}(U,U)=cU$.

2.3. *Analysis*

The gas-kinetic scheme for the linear advection equation has been derived from two initial distribution functions; one is the equilibrium state g expanded across the cell boundary, and the other is the initial nonequilibrium distribution function f_0 expanded at both sides of the cell boundary. In the following, four limiting cases based on the above scheme will be analyzed.

Case (1). In the hydrodynamic limit, the collision time τ is usually much smaller than the CFL time step T ($\tau \ll T$). To first order in τ, Eq. (13) reduces to

$$\begin{aligned}\mathcal{F}(x_{j+1/2},t)=&\left(1-\frac{t}{T}\right)c\overline{U}+\left(-\frac{\tau}{2\lambda}-tc^2+\frac{t\tau c^2}{T}\right)\bar{a}\overline{U}\\&+\frac{t}{2T}\operatorname{erfc}(-\sqrt{\lambda}c)c\overline{U}_l+\frac{t}{2T}\operatorname{erfc}(\sqrt{\lambda}c)c\overline{U}_r\\&-\frac{t\tau}{2T}\left(\operatorname{erfc}(-\sqrt{\lambda}c)c^2+\frac{c}{\sqrt{\pi\lambda}}e^{-\lambda c^2}\right)a^l\overline{U}_l\\&-\frac{t\tau}{2T}\left(\operatorname{erfc}(\sqrt{\lambda}c)c^2-\frac{c}{\sqrt{\pi\lambda}}e^{-\lambda c^2}\right)a^r\overline{U}_r.\end{aligned} \tag{14}$$

In smooth regions, the assumption that $g^l=g^r$ in f_0 is a good approximation. Under these circumstances, Eq. (14) can be further simplified as

$$\mathcal{F}(x_{j+1/2},t)=c\overline{U}-tc^2\bar{a}\overline{U}-\frac{\tau}{2\lambda}\bar{a}\overline{U}. \tag{15}$$

This flux, which has been derived from the solution of the BGK equation (13), is identical to the numerical flux in the one-step Lax–Wendroff scheme for the viscous advection equation of $U_t+cU_x=\nu U_{xx}$ with $\nu=\tau/2\lambda$. If we also take $\overline{U}=(U_j+U_{j+1})/2$ and $\bar{a}=(U_{j+1}-U_j)/\overline{U}$, the final flux of Eq. (15) can be written as

$$\mathcal{F}(x_{j+1/2},t)=\frac{F_j+F_{j+1}}{2}-tc^2(U_{j+1}-U_j)-\nu(U_{j+1}-U_j),$$

with $F_j=cU_j$. The first term on the right-hand side of this equation is the usual Euler flux, while the second one is the flux needed to account for the Lax–Wendroff procedure. The third term is the artificial dissipation flux if we require $U_t+cU_x=0$ as our model equation. However, if we want to solve the viscous equation $U_t+cU_x=\nu U_{xx}$ then the third term represents the physical viscous flux. Actually, this is the precise reason why the BGK model can give an account of the Navier–Stokes solutions. As we know, the Lax–Wendroff scheme gives oscillatory solutions in the strong discontinuity regions if ν is not large enough (the discontinuity thickness is much less than the grid size Δx). An additional dissipation must be added to improve the accuracy. If the temporal resolution is reduced by taking $\mathcal{F}(x_{j+1/2},t)=\mathcal{F}(x_{j+1/2},0)$, then one obtains the Lax–Friedrichs scheme by setting $\tau/\lambda=\Delta x/c\Delta t$. Therefore, the Lax–Friedrichs scheme can be also understood in terms of gas-kinetics, where the flow variable τ/λ is related to the grid size and time step.

Case (2). When τ goes to ∞, the BGK model reduces to the collisionless Boltzmann equation

$$f_t+uf_x=0.$$

In this case, instead of Eq. (12), the solution of f at the cell boundary ($x=0$) is

$$f=f_0(-ut),$$

with

$$f_0(-ut)=\begin{cases}g^l(1-a^lut), & u>0\\ g^r(1-a^rut), & u<0.\end{cases} \tag{16}$$

Only the last term in Eq. (12) is kept in this equation. Physically, the collisionless Boltzmann solution should give very large viscosity, since the particles could always remain in an extreme non-equilibrium state. However, the enforcement of two Maxwellians for f_0 at the beginning of each time step (Eq. (16)) effectively reduces the viscosity. But, the permanent two half-Maxwellians would always keep a certain amount of viscosity in the scheme. This is highly undesirable for Navier–Stokes solutions. Currently, most Boltzmann-type upwind schemes are based on the solution of the collisionless Boltzmann equation [8, 30, 32,

27, 10], and have an intrinsic connection with the flux vector splitting schemes [26]. In order to distinguish more precisely the collisionless Boltzmann equation and the BGK model, it is useful to compare the numerical fluxes which they produce in first-order accurate formulations. The flux for the collisionless Boltzmann equation can be formulated as

$$F^{\text{cll}}_{j+1/2} = \frac{(F_j + F_{j+1})}{2} + d^{\text{cll}}_{j+1/2},$$

where $d^{\text{cll}}_{j+1/2}$ is the diffusion term. This can be written as

$$d^{\text{cll}}_{j+1/2} = \left[\tfrac{1}{2}c(1 - \text{erfc}(\sqrt{\lambda}c)) + \frac{e^{-\lambda c^2}}{2\sqrt{\pi\lambda}}\right](U_j - U_{j+1}).$$

On the other hand, from the BGK model, the corresponding diffusive flux is

$$d^{\text{bgk}}_{j+1/2} = \left[\tfrac{1}{2}c(1 - \text{erfc}(\sqrt{\lambda}c)) + e^{-t/\tau}\frac{e^{-\lambda c^2}}{2\sqrt{\pi\lambda}}\right](U_j - U_{j+1}).$$

The condition for the scheme to be local extremum diminishing (LED) [20] is that the coefficient of $U_{j+1} - U_j$ equals or exceeds $c/2$. This is always satisfied by $d^{\text{cll}}_{j+1/2}$ since

$$1 \geq \sqrt{\pi} m e^{m^2}\text{erfc}(m)$$

holds for all $m = \sqrt{\lambda}|c|$ (*Note.* m is the equivalent Mach number since the equivalent speed of sound is proportional to the square root of the temperature $1/\lambda$). In contrast, the scheme obtained from the collisionless Boltzmann equation could never reduce to the least dissipative first-order LED scheme,

$$F_{j+1/2} = \begin{cases} cU_j, & \text{if } c > 0, \\ cU_{j+1}, & \text{if } c < 0. \end{cases}$$

This would require that $\sqrt{\pi} m e^{m^2}\,\text{erfc}(m) = 1$ which is only possible for an infinitely large Mach number m. From the BGK model, the least dissipative scheme can be obtained easily at finite gas Mach number by choosing the gas relaxation rate $e^{-t/\tau}$ to depend on the Mach number. This can be achieved by setting $e^{-t/\tau} = \sqrt{\pi} m e^{m^2}\,\text{erfc}(m)$. Thus, the BGK model gives a less dissipative scheme than the collisionless Boltzmann equation.

Case (3). In order to get a time-independent flux formulation, all the high-order time-dependent terms in Eq. (12) might be dropped, and the final gas distribution function f is simplified as

$$f = (1 - e^{-t/\tau})g_0 + e^{-t/\tau}f_0,$$

with

$$f_0 = \begin{cases} g^l, & u > 0 \\ g^r, & u < 0. \end{cases}$$

In the above scheme, f_0 is first determined from the limited interpolations of $\overline{U}_l$ and $\overline{U}_r$ in Eq. (7), and $\overline{U}$ in g_0 is obtained from f_0 using Eq. (10). The final numerical flux can be written as

$$F_{j+1/2} = \frac{(c\overline{U}_l + c\overline{U}_r)}{2} + d_{j+1/2},$$

where $d_{j+1/2}$ is a diffusion term:

$$d_{j+1/2} = \left[\tfrac{1}{2}c(1 - \text{erfc}(\sqrt{\lambda}c)) + e^{-t/\tau}\frac{e^{-\lambda c^2}}{2\sqrt{\pi\lambda}}\right](\overline{U}_l - \overline{U}_r).$$

Also, from the analysis in Case (2), $e^{-t/\tau}$ can be estimated from the local flow variables. One choice is to take it as a function of local Mach number, namely

$$e^{-t/\tau} = \sqrt{\pi} m e^{m^2}\text{erfc}(m),$$

where $m = \sqrt{\lambda}|c|$. In this case, the least dissipative high-order upwind scheme is recovered, which is

$$F_{j+1/2} = \begin{cases} c\overline{U}_l & \text{if } c > 0, \\ c\overline{U}_r, & \text{if } c < 0. \end{cases}$$

Case (4). When the complete numerical flux formulation (13) is used for the solution of the viscous advection equation, τ should be composed of two parts:

$$\tau = 2\lambda(\nu_p + \nu_a).$$

Here ν_p is the real physical viscosity, and ν_a is the artificial one. The reason for the artificial viscosity is to satisfy the numerical requirement that the discontinuity thickness δl should not be smaller than one cell size Δx. The increment of τ in the discontinuity region will automatically enlarge the physical thickness δl so as to match the grid size Δx.

The gas-kinetic scheme developed for the advection equation in this section falls between the Lax–Wendroff (from equilibrium state g) and flux–vector splitting schemes (from the nonequilibrium initial distribution f_0). The final flux represents a complicated nonlinear coupling between these two limits through the collision time τ.

The same technique presented in this section could also be used for other hyperbolic equations, provided that an equivalent BGK model can be constructed. For example, $f_t + uf_x = (f - g)/\tau$ with an equilibrium state g of $g = U\sqrt{\lambda/\pi}e^{-\lambda(u-U/2)^2}$ can be applied to solve the viscous Burg-

ers' equation

$$U_t + (U^2/2)_x = \nu U_{xx}$$

with $\nu = \tau/2\lambda$. Also, the three-dimensional linear advection equation [36]

$$U_t + aU_x + bU_y + cU_z = 0$$

can be solved using the BGK model $f_t + uf_x + vf_y + wf_z = (g - f)/\tau$, assuming the equilibrium distribution

$$g = \sqrt{(\lambda/\pi)^{3/2}} U e^{-\lambda[(u-a)^2+(v-b)^2+(w-c)^2]}.$$

3. GAS-KINETIC SCHEMES FOR 3D HYDRODYNAMIC EQUATIONS

The numerical flux obtained using the gas-kinetic formulation for the linear advection equation appears much more complicated than those obtained from other standard central difference or upwind schemes. The real advantage of the gas-kinetic approach over more conventional methods is realized when one considers the Euler and Navier–Stokes equations. In fact, by requiring only a single scalar gas distribution function f, the gas-kinetic approach greatly simplifies the calculation of mass, momentum, energy densities, and their fluxes.

Gas-kinetic schemes developed from the BGK model have been successfully applied to 1D and 2D flows [48]. In this section, we construct a novel 3D method and extend the analysis of the previous section to systems of conservation laws. In particular, the extension of the method analyzed in Case (3) of the previous section yields a very interesting discretization scheme for the steady Euler equations.

Furthermore, we will show that the proposed gas-kinetic scheme satisfies the entropy condition (i.e., the so-called H-theorem).

3.1. *Finite Volume Gas-Kinetic Scheme in Three Dimension*

In the finite volume method [18, 19], the discretization is accomplished by dividing the flow into a large number of small subdomains and by applying the conservation laws in the integral form

$$\frac{d}{dt}\int_\Omega U\, dV + \int_{\partial\Omega} \mathbf{F}\cdot d\mathbf{S} = 0 \tag{17}$$

to each subdomain Ω with boundary $\partial\Omega$. In this equation U is the mascroscopic state vector, defined as

$$U = \begin{pmatrix} \rho \\ P_x \\ P_y \\ P_z \\ \varepsilon \end{pmatrix} \tag{18}$$

where ρ, $\vec{P}$ and ε are the mass, momentum, and energy densities, and $\mathbf{F}$ is the flux vector with components F_x,F_y, and F_z in the three coordinate directions. In a gas-kinetic finite volume scheme the flux vectors across cell boundaries are constructed by computing the gas distribution function f. In three dimensions, the governing equation for f is described by the BGK model [3], which is

$$f_t + uf_x + vf_y + wf_z = (g - f)/\tau, \tag{19}$$

where f is a function of space (x, y, z), time t, particle velocity (u, v, w), and internal variable ξ with K degrees of freedom (i.e., $K = 2$ for $\gamma = 1.4$ gases in 3D). The relations between mass ρ, momentum $\vec{P}$, and energy ε densities with the distribution function f are

$$\begin{pmatrix} \rho \\ P_x \\ P_y \\ P_z \\ \varepsilon \end{pmatrix} = \int \psi_\alpha f\, d\Xi, \quad \alpha = 1, 2, ..., 5, \tag{20}$$

where ψ_α is the vector of moments

$$\psi_\alpha = (1, u, v, w, \tfrac{1}{2}(u^2 + v^2 + w^2 + \xi^2))$$

and $d\Xi = du\, dv\, dw\, d\xi$ is the volume element in the phase space [45]. The equilibrium state g in the BGK model has a Maxwellian distribution of

$$g = Ae^{-\lambda((u-U)^2+(v-V)^2+(w-W)^2+\xi^2)},$$

where U, V, and W are macroscopic gas velocities. For an equilibrium gas flow with $f = g$, the Euler equations in three-dimensional space can be obtained by taking the moments of ψ_α in Eq. (19). On the other hand, to the first order of τ, the Navier–Stokes equations, with a dynamic viscosity coefficient of τp (where p is the pressure), can be derived from the Chapman–Enskog expansion [4]. Since mass, momentum, and energy are conservative quantities in the process of gas evolution, f and g have to satisfy the conservation constraint of

$$\int (g - f)\psi_\alpha\, d\Xi = 0, \quad \alpha = 1, 2, ..., 5, \tag{21}$$

at any point in space and time.

The general solution for f in Eq. (19) in three dimensions at the position of (x, y, z) and t is

$$f(x, y, z, t, u, v, w, \xi) = \frac{1}{\tau}\int_0^t g(x', y', z', t, u, v, w, \xi) e^{-(t-t')/\tau} dt' + e^{-t/\tau} f_0(x - ut, y - vt, z - wt), \tag{22}$$

where $x' = x - u(t - t')$, $y' = y - v(t - t')$, $z' = z - w(t - t')$ are the trajectory of a particle motion, and f_0 is the initial nonequilibrium gas distribution function f at the beginning of each time step ($t = 0$). Two unknowns g and f_0 must be determined in the above equation to obtain the solution f. In order to calculate the evolution of the macroscopic quantities in Eq. (20), Eq. (19) can be integrated over u, v, w, x, y, z, and t for a control volume defined by a mesh cell and a time step T. This requires the evaluation of fluxes across cell boundaries. We will consider the evaluation of fluxes across a boundary separating two cells in the x direction and, to simplify the notation, the point for evaluating fluxes at the cell boundary will be assumed at ($x = 0$, $y = 0$, $z = 0$).

Generally, f_0 and g can be expanded around the cell boundary as

$$f_0 = \begin{cases} g^l(1 + a^l x + b^l y + c^l z), & x < 0, \\ g^r(1 + a^r x + b^r y + c^r z), & x > 0, \end{cases} \tag{23}$$

and

$$g = g_0(1 + \bar{a}x + \bar{b}y + \bar{c}z + \bar{A}t), \tag{24}$$

where g^l, g^r, and g_0 are local Maxwellian distribution functions. The dependence of a^l, b^l, ..., $\bar{A}$ on the particle velocity can be obtained from the Taylor expansion of a Maxwellian, which have the form

$$\begin{aligned} a^l &= a_1 + a_2 u + a_3 v + a_4 w + a_5(u^2 + v^2 + w^2 + \xi^2), \\ &\cdots \\ \bar{A} &= \bar{A}_1 + \bar{A}_2 u + \bar{A}_3 v + \bar{A}_4 w \\ &\quad + \bar{A}_5(u^2 + v^2 + w^2 + \xi^2), \end{aligned} \tag{25}$$

where all coefficients of $a_1, a_2, ..., \bar{A}_5$ are local constants. The idea of interpolating f_0 separately at the regions of $x < 0$ and $x > 0$ follows from physical considerations: for a non-equilibrium gas flow, the physical quantities can change dramatically from place to place, such as across a shock front where the upstream and downstream gas distribution function f could be different Maxwellians. In the 1960s, the idea of using two Maxwellians had been successfully applied in many problems, such as the calculations of shock structure and Couette flows [21, 4].

In the following, the SLIP formulation [20], similar to that used for the linear advection equation, will be used for the interpolations of all initial mass, momentum, and energy densities in the x, y, and z directions, respectively. After implementing the limiters, the macroscopic variables can be obtained in the left ($x < 0$) and right sides ($x > 0$) separately,

$$\begin{aligned} \bar{\rho} &= \rho_0 + \rho_1 x + \rho_2 y + \rho_3 z \\ \bar{P}_x &= P_{x0} + P_{x1} x + P_{x2} y + P_{x3} z \\ \bar{P}_y &= P_{y0} + P_{y1} x + P_{y2} y + P_{y3} z \\ \bar{P}_z &= P_{z0} + P_{z1} x + P_{z2} y + P_{z3} z \\ \bar{\varepsilon} &= \varepsilon_0 + \varepsilon_1 x + \varepsilon_2 y + \varepsilon_3 z, \end{aligned} \tag{26}$$

where $\rho_0, \rho_1, ..., \varepsilon_3$ are local constants. The expansions (23) and (26) are substituted into the moment equation (20)) to yield

$$\begin{pmatrix} \bar{\rho} \\ \bar{P}_x \\ \bar{P}_y \\ \bar{P}_z \\ \bar{\varepsilon} \end{pmatrix} = \int \psi_\alpha f_0 \, d\Xi, \quad \alpha = 1, 2, ..., 5, \tag{27}$$

All the coefficients in f_0 can be obtained directly. Then, g_0 in Eq. (24) at ($x = 0$, $y = 0$, $z = 0$, $t = 0$) can be evaluated automatically by taking the limit of Eq. (22) as $t \to 0$ and substituting it into Eq. (21) to obtain

$$\begin{aligned} \int g_0 \psi_\alpha \, d\Xi = &\int_{u>0} \int g^l \psi_\alpha \, d\Xi \\ &+ \int_{u<0} \int g^r \psi_\alpha \, d\Xi, \quad \alpha = 1, 2, ..., 5. \end{aligned} \tag{28}$$

This stage is different from the method which was previously used [29, 47] to obtain g_0.

The other terms of $\bar{a}$, $\bar{b}$, and $\bar{c}$ in Eq. (24) at $t = 0$ can be computed from the new mass, momentum, and energy interpolations which are continuous across the cell boundary in all three directions. Now, the only unknown term left in Eq. (24) is $\bar{A}$. This can be evaluated as follows by substituting Eq. (23) and Eq. (24) into Eq. (22); we get

$$\begin{aligned} f(0, 0, 0, t, u, v, w, \xi) = &(1 - e^{-t/\tau}) g_0 \\ &+ (\tau(-1 + e^{-t/\tau}) \\ &+ te^{-t/\tau})(u\bar{a} + v\bar{b} + w\bar{c}) g_0 \\ &+ \tau(t/\tau - 1 + e^{-t/\tau}) \bar{A} g_0 \\ &+ e^{-t/\tau} f_0(-ut, -vt, -wt), \end{aligned} \tag{29}$$

with

$$f_0(-ut, -vt, -wt) = \begin{cases} g^l(1 - a^l ut - b^l vt - c^l wt), & u > 0, \\ g^r(1 - a^r ut - b^r vt - c^r wt), & u < 0. \end{cases}$$

Both f (Eq. (29)) and g (Eq. (24)) contain $\bar{A}$. After applying the condition (21) at $(x = 0, y = 0, z = 0)$ and integrating it over the whole time step T, such as

$$\int_0^T \int (g - f)\psi_\alpha \, d\Xi \, dt = 0, \tag{30}$$

five moment equations of $\bar{A}$ can be obtained, from which the five constants in $\bar{A}$ of Eq. (25) can be uniquely determined. Finally, the time-dependent numerical fluxes in the x-direction across the cell boundary can be computed as

$$F_x = \begin{pmatrix} \mathcal{F}_\rho \\ \mathcal{F}_{P_x} \\ \mathcal{F}_{P_y} \\ \mathcal{F}_{P_z} \\ \mathcal{F}_\varepsilon \end{pmatrix} = \int u \begin{pmatrix} 1 \\ u \\ v \\ w \\ \frac{1}{2}(u^2 + v^2 + w^2 + \xi^2) \end{pmatrix} f(0, 0, 0, t, u, v, w, \xi) \, d\Xi. \tag{31}$$

The corresponding fluxes F_y and F_z in the y and z directions are similarly obtained by taking moments with v and w, respectively. These fluxes satisfy the consistency condition $\mathcal{F}(U, U) = \mathcal{F}(U)$ for a homogeneous uniform flow, where $\mathcal{F}(U)$ is identical to the corresponding Euler fluxes in the 3D case.

3.2. *Analysis*

Equation (29) gives explicitly the time-dependent gas distribution function f at the cell boundary. In order to understand this formulation, several limiting cases will be discussed below.

Case (1). In the hydrodynamic limit of $\tau \ll T$ and in the smooth region of $g^l = g^r$, to first order in τ, Eq. (29) can be simplified as

$$f = g_0(1 - \tau(u\bar{a} + v\bar{b} + w\bar{c}) + (t - \tau)\bar{A}). \tag{32}$$

Substituting Eq. (32) into the flux formula (Eq. (31)), schemes which are identical to these obtained from the one-step Lax–Wendroff scheme for the Navier–Stokes equations can be recovered. Also, from the gas kinetic theory, the stress tensor is defined as

$$\tau_{ij} = \int (u_i - U_i)(u_j - U_j) f \, d\Xi.$$

For example, using the distribution function f in Eq. (32), the shear stress τ_{xy} can be obtained exactly as

$$\tau_{xy} = \tau p \left(\frac{\partial U}{\partial y} + \frac{\partial V}{\partial x} \right),$$

where τp is the dynamic viscosity coefficient and p is the local pressure. Thus, the current scheme can accurately represent the Navier–Stokes solutions in the smooth flow regions, if the initial data, such as $\partial U/\partial y$ and $\partial V/\partial x$, are interpolated correctly, since all these terms are included in the final flux formulation through the terms containing $\bar{a}$, $\bar{b}$, and $\bar{c}$. The actual one-step Lax–Wendroff type scheme for the Navier–Stokes equations is rarely applied, because it requires the evaluation of many Jacobian matrices. Therefore, in practice, two-step methods, such as the two-step predictor and corrector schemes [33, 22] have generally been preferred. However, with the gas-kinetics formulation, the matrix transformations are not difficult and the Navier–Stokes fluxes can be simply obtained without separating the viscous and advection terms. In fact, Eq. (32) has been used successfully for subsonic boundary layer and slight compressible turbulent flow calculations [48].

Case (2). In the limit of $\tau = \infty$ corresponding to the collisionless Boltzmann equation, the solution of the gas distribution function f in Eq. (29) reduces to

$$f = f_0(x - ut, y - vt, z - wt),$$

where only the last term in Eq. (29) is kept. The final numerical fluxes in this case can be computed as

$$\begin{pmatrix} \mathcal{F}_\rho \\ \mathcal{F}_{P_x} \\ \mathcal{F}_{P_y} \\ \mathcal{F}_{P_z} \\ \mathcal{F}_\varepsilon \end{pmatrix} = \int_{u>0} \int u \begin{pmatrix} 1 \\ u \\ v \\ w \\ \frac{1}{2}(u^2 + v^2 + w^2 + \xi^2) \end{pmatrix} g^l(1 - a^l ut - b^l vt - c^l wt) \, d\Xi$$
$$+ \int_{u<0} \int u \begin{pmatrix} 1 \\ u \\ v \\ w \\ \frac{1}{2}(u^2 + v^2 + w^2 + \xi^2) \end{pmatrix} g^r(1 - a^r ut - b^r vt - c^r wt) \, d\Xi. \tag{33}$$

This formulation is intrinsically upwind through the representation of particle motion and it is precisely the kinetic representation of flux vector splitting for the Euler equations [12, 35, 39].

Mandal and Deshpande [26] show that the kinetic flux vector splitting (KFVS) derived from Eq. (33) is equivalent to the flux vector splitting of van Leer [43]. Macrossan [24] and Deshpande [8] note that KFVS has grid-dependent numerical viscosities and gives excessively dissipative results. Also, the analysis for the linear advection equation in Section 2 of this paper shows that the corresponding first-order KFVS that will never give the least dissipative upwind scheme. For the Navier–Stokes solutions, the excessive and unavoidable dissipation originating from the two half-Maxwellians in KFVS produces a deterioration in the accuracy of the numerical results [44], in which an abnormally large numerical mixing of the fluid occurs within the boundary, or a fictitious pressure gradient is created that causes an unrealistic convection within the layer [23]. On the other hand, the collisional BGK model provides a mechanism to reduce the intrinsic dissipation and can give accurate Navier–Stokes solutions [47].

Case (3). The full Boltzmann scheme gives time-dependent fluxes, which might handicap the convergence of the scheme to a steady state. Thus, for steady state calculations, the relaxation process must be simplified in order to yield constant numerical fluxes. The easiest way to achieve this is to ignore all high-order spatial and temporal terms in the expansion of f and g. So, instead of Eq. (23) and Eq. (24), we use

$$f_0 = \begin{cases} g^l, & x < 0, \\ g^r, & x > 0, \end{cases}$$

and

$$g = g_0$$

as the initial nonequilibrium gas distribution f_0 and the equilibrium state g. Substituting the above two equations into Eq. (22), the solution of f at the cell boundary can be obtained as

$$f(0, 0, 0, t) = (1 - e^{-t/\tau})g_0 + e^{-t/\tau}f_0. \tag{34}$$

The idea of obtaining g_0 from f_0 has been independently proposed both in the total thermalized transport (TTT) scheme [48] and in the equilibrium interface method (EIM) [25]. But in the latter method, the final Euler fluxes are simply evaluated from the equilibrium state g_0, which could lead to difficulties in the transonic flow regime; since the real gas distribution function f should stay in a nonequilibrium and physically dissipative state at a shock front. On the other hand, the physical BGK model (34) always gives a relaxation process, which can recover the nonequilibrium gas behavior at discontinuities. Equation (34) can be rewritten as

$$f = g_0 + e^{-t/\tau}(f_0 - g_0). \tag{35}$$

The first term on the right represents the Euler-fluxes. The second is a diffusive term, which should be large near discontinuities in order to keep f in a nonequilibrium state. This term is both necessary to prevent numerical oscillations and physically correct in that it accounts for the nonequilibrium behavior of the gas flow in the discontinuity region. This requirement makes $e^{-t/\tau}$ have the same functional effect as the parameter $\varepsilon^{(2)}$ in the JST scheme [16], which is controlled by a nonlinear limiting process. Thus a scheme similar to the JST scheme, with the Euler fluxes augmented by adaptive diffusive terms, is obtained from a simplified gas-kinetic formulation. Note that in the gas-kinetic scheme formulation diffusion is caused by the imbalance between the equilibrium and nonequilibrium states rather than the difference between the left and right states. Formally, Eq. (35) can be written as

$$f = g_0 + \varepsilon^{(2)}(f_0 - g_0), \tag{36}$$

where $\varepsilon^{(2)}$ is the adaptive coefficient. In the implementation of this scheme we first construct f_0 from the interpolated macroscopic mass, momentum, and energy densities at both sides of a cell boundary using Eq. (26), where x, y, and z dependent terms are ignored and the equilibrium state g_0 is obtained from f_0 using Eq. (28). As in the case of time dependent calculations, the accuracy is improved by the use of higher order interpolation with the SLIP formulation to estimate the local constants for the left and right states, so that in smooth regions, where the limiters are not active, the magnitude of $f_0 - g_0$ is reduced.

3.3. *The Entropy Theorem*

At this point, it would be interesting to investigate whether the Boltzmann scheme satisfies the entropy condition. It is well-known that a method satisfying the entropy condition prevents the formation of expansion shocks. The H-theorem, which has been described in the kinetic theory of gases as the bridge connecting equilibrium thermodynamics with non-equilibrium statistical mechanics, states that the H-function defined by $H = \int f \ln f \, d\Xi$ monotonically decreases with time as a homogeneous gas in statistical non-equilibrium evolves to equilibrium. In the case of inhomogeneity, the theorem states that

$$\frac{\partial H}{\partial t} + \frac{\partial H_i}{\partial x_i} \leq 0, \tag{37}$$

where H_i is the H-flux defined by

$$H_i = \int u_i f \ln f \, d\Xi.$$

In the last section, we have computed the time-dependent gas distribution function f at a cell boundary (Eq. (29)). Substituting Eq. (29) into the entropy equation (37), and

integrating over a time step $\Delta t = T$, the numerical scheme satisfies

$$\begin{aligned}
\int_0^{\Delta t}\left(\frac{\partial H}{\partial t}+\frac{\partial H_i}{\partial x_i}\right)dt &= \int_0^{\Delta t}\int (f_t + u_i f_{x_i})\,d\Xi\,dt \\
&\quad + \int_0^{\Delta t}\int (f_t + u_i f_{x_i})\ln f\,d\Xi\,dt \\
&= \frac{1}{\tau}\int_0^{\Delta t}\int (g-f)\,d\Xi\,dt \\
&\quad + \frac{1}{\tau}\int_0^{\Delta t}\int (g-f)\ln f\,d\Xi\,dt \\
&= \frac{1}{\tau}\int_0^{\Delta t}\int (g-f)(\ln f - \ln g)\,d\Xi\,dt \\
&\quad + \frac{1}{\tau}\int_0^{\Delta t}\int (g-f)\ln g\,d\Xi\,dt \\
&\leq \frac{1}{\tau}\int_0^{\Delta t}\int (g-f)\ln g\,d\Xi\,dt \\
&= \frac{1}{\tau}\int_0^{\Delta t}\int (g-f)(\ln g_0 \\
&\quad + \ln(1+\overline{A}t))\,d\Xi\,dt \\
&= \frac{1}{\tau}\int_0^{\Delta t}\int (g-f)\ln(1+\overline{A}t)\,d\Xi\,dt \\
&= \frac{1}{\tau}\int_0^{\Delta t}\int (g-f)\overline{A}t\,d\Xi\,dt + \vartheta_1(\Delta t)^3 \\
&= 0 + \vartheta_2(\Delta t)^3.
\end{aligned}$$

Here the property $\int_0^{\Delta t}\int (g-f)\psi_\alpha\,d\Xi\,dt = 0$ in Eq. (30) has been used to establish that

$$\int_0^{\Delta t}\int (g-f)\,d\Xi\,dt = 0$$

$$\int_0^{\Delta t}\int (g-f)\ln g_0\,d\Xi\,dt = 0$$

$$\int_0^{\Delta t}\int (g-f)\overline{A}\,d\Xi\,dt = 0$$

since 1, $\ln g_0$ and $\overline{A}$ can each be expanded as a combination of the components of the conservative moments ψ_α. These properties are satisfied numerically in this scheme in the evaluation of $\overline{A}$. Thus we conclude that, to second-order accuracy, our scheme satisfies the H-theorem on the average of the whole time step. The additional term of $\vartheta(\Delta t)^3$ stems from the fact that the Taylor expansions (Eq. (24)) make the actual equilibrium state g deviate from the exact Maxwellian at the location away from the origin of the expansion at ($x = 0, y = 0, z = 0$) and ($t = 0$). Otherwise, the H-theorem could be satisfied exactly. However, for the simplified relaxation scheme of Eq. (35), the H-theorem is satisfied exactly. Also, it can be proved that the entropy ($S = -kH$, k is the Boltzmann constant) of g_0 is always larger than that of f_0, which is

$$\begin{aligned}
\Delta H &= \int g_0 \ln g_0\,d\Xi - \int f_0 \ln f_0\,d\Xi \\
&= \int (g_0 - f_0)\ln g_0\,d\Xi + \int f_0(\ln(g_0/f_0)\,d\Xi \\
&= \int f_0 \ln(g_0/f_0)\,d\Xi \\
&\leq \int f_0(g_0/f_0 - 1)\,d\Xi \\
&= \int (g_0 - f_0)\,d\Xi \\
&= 0.
\end{aligned}$$

This property guarantees that the local physical system will approach the state with larger entropy, and prevents the formation of unphysical rarefaction shocks.

4. NUMERICAL EXAMPLES

4.1. Unsteady Flow Calculations

In [48], many 1D and 2D test cases have been presented for the numerical Euler and Navier–Stokes solutions using an earlier gas-kinetic scheme based on the solution of the BGK equation. It appears that this scheme can give an accurate result for problems with a strong rarefaction wave in the high-speed low density regions, such as for the Sjögreen test [9]. Actually, this is not surprising, since all particles with velocities from $-\infty$ to $+\infty$ have been considered in the process of computing numerical fluxes. Whereas many other schemes simply use Mach number as a criterion to determine the directions of gas movement.

In all the following, we will apply the scheme developed in this paper to well-known test cases. In all calculations, the van Leer limiter

$$L(u, v) = S(u, v)\frac{2|u|\,|v|}{|u| + |v|}, \tag{38}$$

with $S(u, v) = 1/2\{\text{sign}(u) + \text{sign}(v)\}$, is used in the SLIP scheme for all interpolations of the conservative variables in Eq. (26).

We first apply our new Boltzmann scheme (Eq. (31)) to five unsteady test cases, which include Sjögreen and slowly moving shock tests in 1D, as well as strong diffracting shock, uniform Mach 3 flow in a channel with a forward-facing step and double Mach reflection cases in 2D [46].

The Sjögreen test is taken from a recently published paper by Einfeldt *et al.* [9]. In that paper, they showed that no scheme whose interface flux derived from a linearized Riemann solution can be positively conservative. But, our new scheme is very nonlinear. The initial data for this case is $\rho_l = 1$, $P_l = -2$, $\varepsilon_l = 3$ and $\rho_r = 1$, $P_r = 2$, $\varepsilon_r = 3$ for the left and right sides initial mass, momentum, and energy densities. Our results are shown in Fig. 1 on a mesh of 200 cells. As we know, many Godunov-type schemes could fail in this problem.

In a well-known paper [34], Roberts found that for slow shocks, there is a significant error generated when using the numerical flux from a solution of Riemann's problem. The error consists of a long wavelength noise in the downstream, which is not effectively damped by the dissipation of the Godunov-type schemes. By page count, Colella and Woodward spend $\frac{1}{3}$ of their paper discussing dissipation mechanisms to try and minimize the problem [7]. Actually, the nature of the shock structure produced by a particular scheme can have a large bearing on how well the scheme copes with slowly moving shock waves. Fortunately, the gas-kinetic model was mostly applied to shock structure calculations. The following test is a problem of a Mach 3 shock wave moving slowly from left to right; the preshock state (density, velocity, pressure) is (1, −3.44, 1) and the postshock state is (3.86, −0.81, 10.33). For a Courant number of one it takes 50 time steps for this shock to traverse one mesh cell. The simulation domain is 200 cells in the x direction, and the original shock is located at the site of the 100th cell. In order to avoid the error generated from the initial interpolation, as Roberts did, we simulate this test using our first-order Boltzmann scheme by ignoring all x-dependent terms in Eq. (26) for 1D interpolations. Figure 2 is a snapshot of the results at 2000 time steps, where the shock has moved about 30 cells to the right. As we can see that the Boltzmann scheme gives a pretty smooth postshock profile.

The next numerical example is a strong shock of Mach number 5.09 diffracting around a corner [31]. Figure 3, Figure 4, and Figure 5 show the mesh, density, and entropy contours by our Boltzmann scheme (Eq. (31)). There are not any detection or entropy-fixes in our calculation. It is also known that the original Godunov scheme, the Roe scheme without the entropy-fix, and the Osher scheme could give a shock at the rarefaction corner.

The forward-facing step test is carried out on a uniform mesh of 240 × 80 cells as shown in Fig. 6 and the numerical results are presented in Fig. 7 and Fig. 8 for the density and entropy distribution. Here, the collision time used is equivalent to a Reynolds number of Re ≃ 50,000 for the upstream gas flow regarding the wind tunnel height as the characteristic length scale. A slip boundary condition is imposed in order to avoid using finer meshes close to the boundary. There is no special treatment around the corner, and we never found any

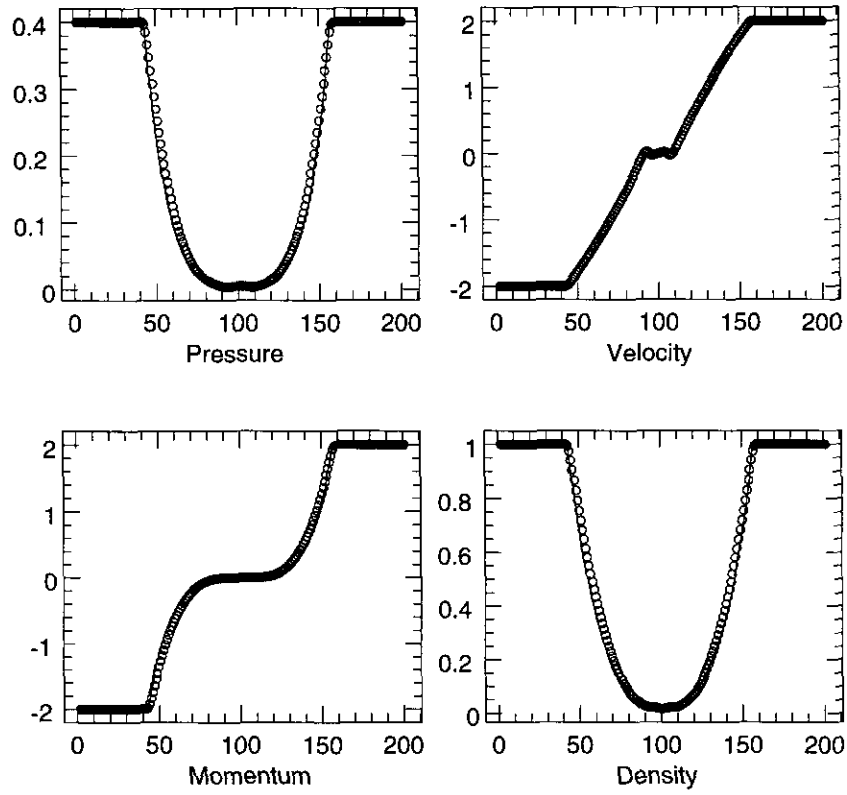

FIG. 1. Sjögreen test for strong rarefaction waves.

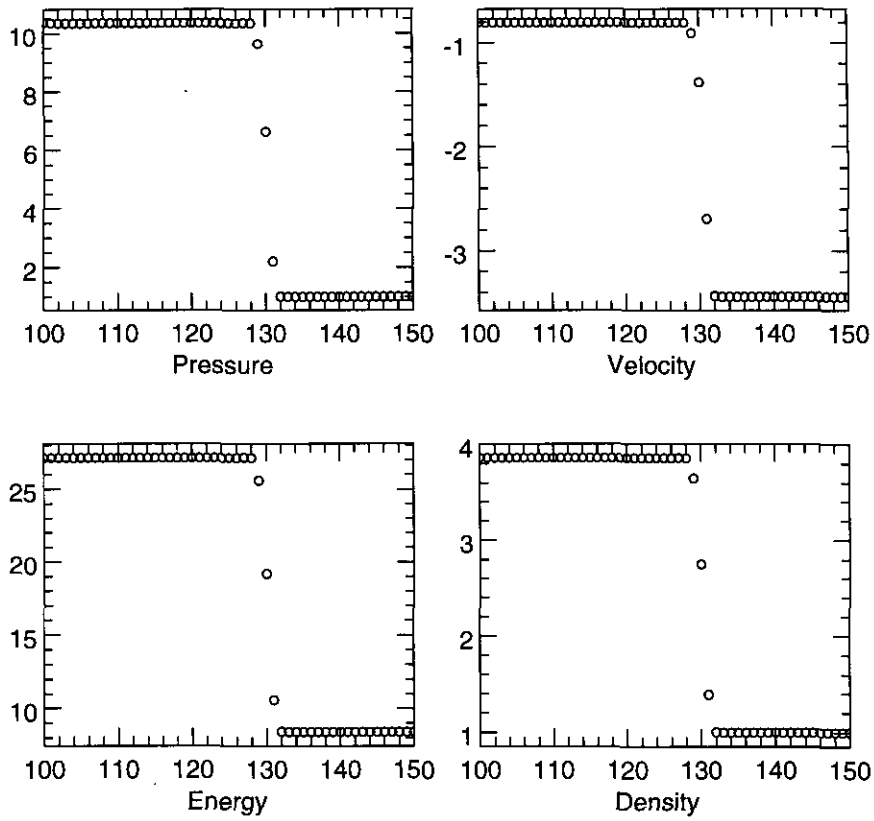

FIG. 2. Slowly moving shock wave calculated by first-order scheme.

expansion shocks emerging from the corner. Also, our numerical experiments verify that the expected qualitative relation between the Reynolds number and the shear instability amplitude, starting from the triple point, is obtained by changing the collision time in the BGK model.

The double Mach reflection of a strong shock test is calculated on the computational domain of 360×120. The problem is set up by driving a shock down a tube which contains a wedge as shown in Fig. 9. The density and entropy distribution after the collision between the shock and the wedge are shown on Fig. 10 and Fig. 11 The same limiter of Eq. (38) is used for all conservative quantities.

All these results confirm the accuracy and high resolution of the gas-kinetic scheme. Complex features, such as oblique shocks and the triple points, are captured without oscillations. We seem to do at least as well as other codes, such as PPM and ENO schemes. The numerical fluxes in our scheme are obtained from a physical microscopic gas evolution model, which avoids uncertainties in the macroscopic equation in extreme conditions, such as discontinuities. For strong rarefaction

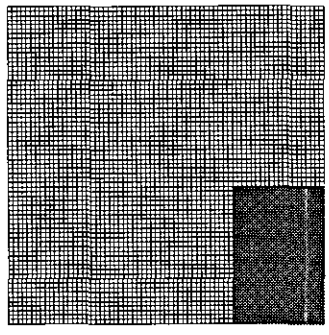

FIG. 3. Mesh distribution of 70×70 for Mach 5.09 diffraction shock test.

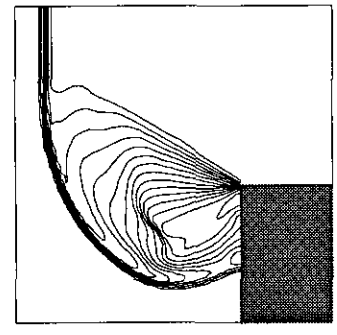

FIG. 4. Density distribution for Mach 5.09 diffraction shock test.

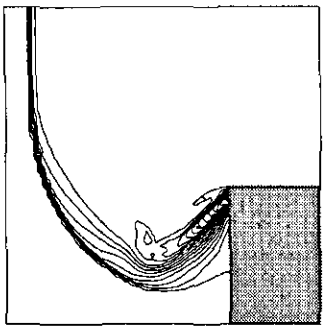

FIG. 5. Entropy distribution for Mach 5.09 diffraction shock test.

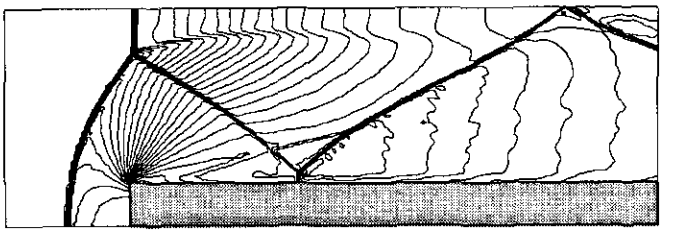

FIG. 7. Density distribution for Mach 3 wind tunnel test on mesh 240 × 80.

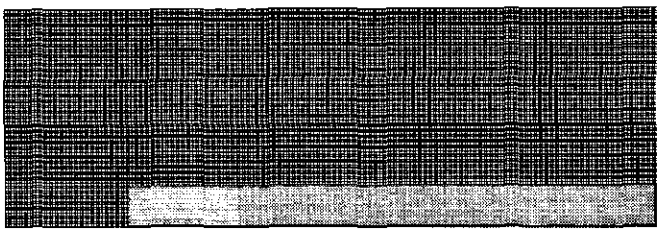

FIG. 6. Mesh distribution of 240 × 80 for Mach 3 wind tunnel test.

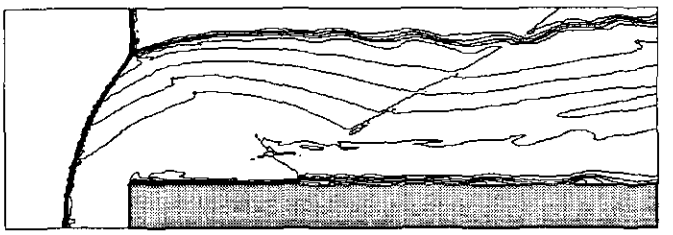

FIG. 8. Entropy distribution for Mach 3 wind tunnel test on mesh 240 × 80.

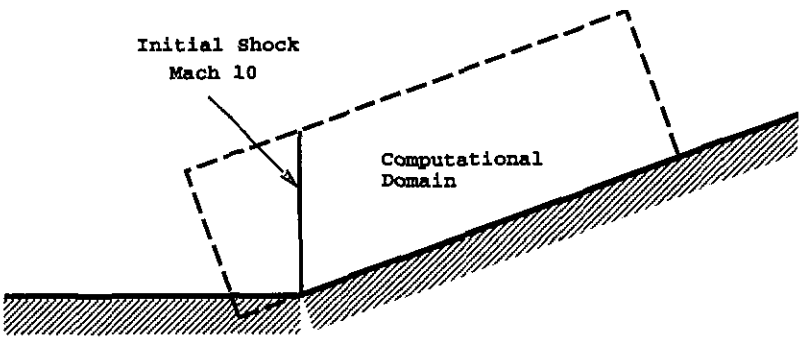

FIG. 9. Mach 10 reflection shock problem.

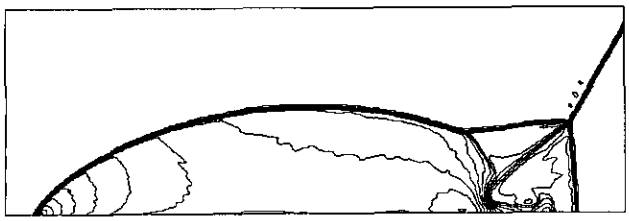

FIG. 10. Density distribution for Mach 10 reflection shock on mesh 360 × 120.

waves, no entropy-fix is needed in our scheme. The gas-kinetic scheme also has the advantage that there are no significant differences between 1D, 2D, and 3D flow calculations.

4.2. *Steady Flow Calculations with Multigrid Acceleration*

The gas-kinetic discretization scheme formulated in Section 3.1, Eq. (17), (18), and (31) has been used to reduce the Euler equations to a semi-discrete form

$$\frac{dw}{dt} + R(w) = 0, \tag{39}$$

where w is the vector of flow variables at the mesh points, and $R(w)$ is the vector of the residuals, consisting of the flux balances augmented by the diffusive terms which are calculated in accordance with Eq. (36). In the case of a steady state calculation the details of the transient solution are immaterial, and the time stepping scheme may be designed solely to maximize the rate of convergence.

If an explicit scheme is used, the permissible time step for stability may be so small that a very large number of time steps are needed to reach a steady state. This can be alleviated by using time steps of varying size in different locations, which are adjusted so that they are always close to the local stability limit. If the mesh interval increases with the distance from the body, the time step will also increase, producing an effect comparable to that of an increasing wave speed. Convergence to a steady state can be further accelerated by the use of a multigrid procedure of the type described below. With the aid of these measures explicit multi-stage schemes have proved extremely effective. Implicit schemes allow much larger time steps, but the work required in each time step may become excessively large, especially in three-dimensional calculations. An explicit five-stage Runge–Kutta scheme with implicit residual averaging and varying local time step is used to drive the multigrid time-stepping scheme [19, 20].

The multigrid scheme is a full approximation scheme defined as follows [17, 19]. Denote the grids by a subscript k. Start with a time step on the finest grid $k = 1$. Transfer the solution from a given grid to a coarser grid by a transfer operator $P_{k,k-1}$, so that the initial state on grid k is

$$w_k^{(0)} = P_{k,k-1} w_{k-1}.$$

Then on grid k the time stepping scheme is reformulated as

$$w_k^{(q+1)} = w_k^{(0)} - \alpha_n \Delta t (R_k^{(q)} + G_k),$$

where the forcing function G_k is defined as the difference between the aggregated residuals transferred from grid $k-1$ and the residual recalculated on grid k. Thus

$$G_k = Q_{k,k-1} R(w_{k-1}) - R(w_k^{(0)}),$$

where $Q_{k,k-1}$ is another transfer operator. On the first stage the forcing term G_k simply replaces the coarse grid residual by the aggregated fine grid residuals. The accumulated correction on a coarser grid is transferred to the next higher grid by an interpolation operator $I_{k-1,k}$ so that the solution on grid $k-1$ is updated by the formula

$$w_{k-1}^{\text{new}} = w_{k-1} + I_{k-1,k}(w_k - w_k^{(0)}).$$

The whole set of grids is traversed in a W cycle in which time steps are only performed when moving down the cycle.

Steady state transonic flow calculations for NACA0012, RAE2822, and Korn airfoils using the simplified relaxation

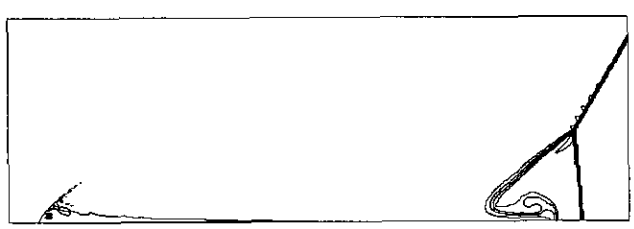

FIG. 11. Entropy distribution for Mach 10 reflection shock on mesh 360 × 120.

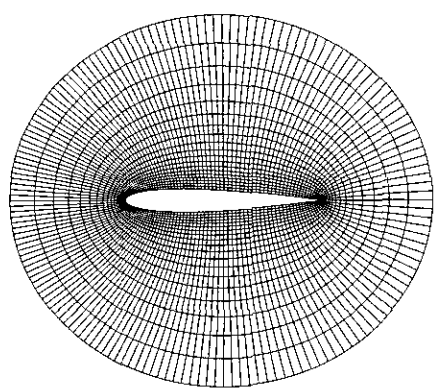

FIG. 12. Mesh for NACA 0012 airfoil.

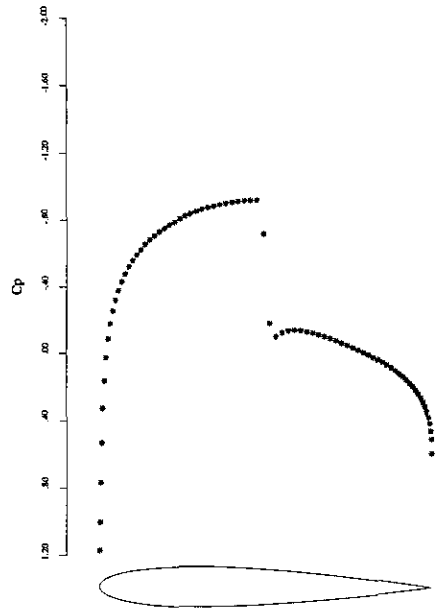

FIG. 13. NACA 0012 with $M = 0.8$, $\alpha = 0.0$, $C_L = 0.000$, $C_D = 0.0079$.

scheme (36) are presented. In these calculations, the selective parameter $\varepsilon^{(2)}$ is determined by a switching function calculated from local pressure gradients. Using subscripts i and j to label the mesh cells, the switching function for fluxes in the i direction is

$$\varepsilon^{(2)} = 1 - e^{-\alpha \cdot \max(P_{i+1,j}, P_{i,j})}. \tag{40}$$

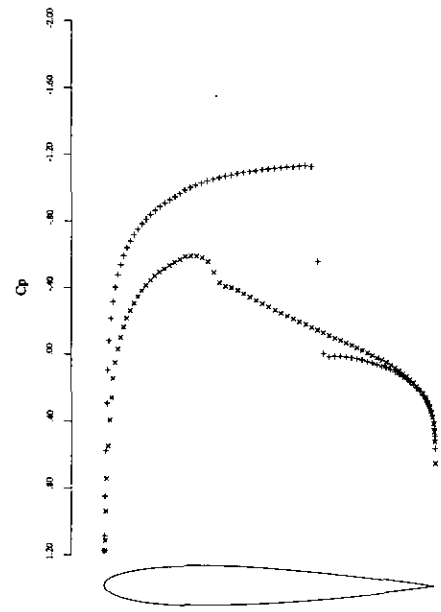

FIG. 14. NACA 0012 with $M = 0.8$, $\alpha = 1.25$, $C_L = 0.3724$, $C_D = 0.0232$.

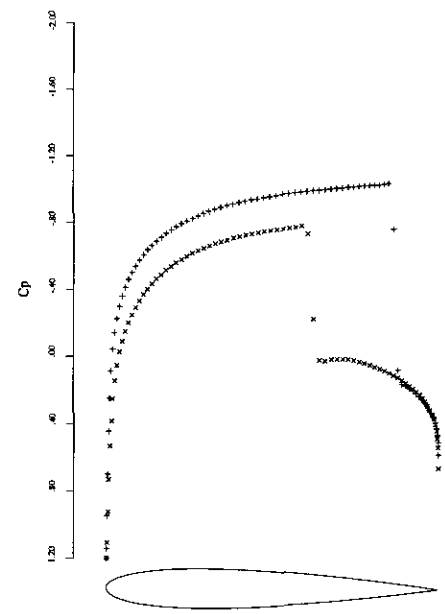

FIG. 15. NACA 0012 with $M = 0.85$, $\alpha = 1.0$, $C_L = 0.3978$, $C_D = 0.587$.

where α is a constant,

$$P_{i,j} = \frac{|\Delta p_{i+1/2,j} - \Delta p_{i-1/2,j}|}{|\Delta p_{i+1/2,j}| + |\Delta p_{i-1/2,j}|},$$

and

$$\Delta p_{i+1/2,j} = p_{i+1,j} - p_{i,j}.$$

In the following calculations, the parameter α in (40) is set to be $\alpha = 0.5$. Also the van Leer limiter is again used in the SLIP formulation for the interpolation of the left and right states. The computational domain is an O-mesh with 160 cells in the circumferential direction and 32 cells in the radial direction. This is a fine enough mesh to produce accurate answers with

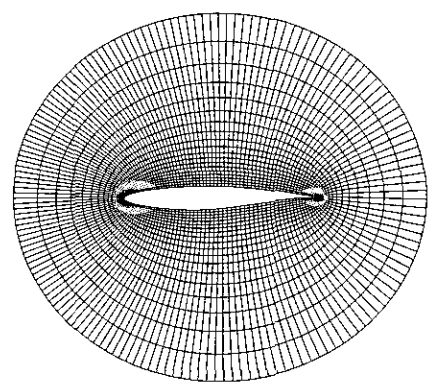

FIG. 16. Mesh for RAE 2822 airfoil.

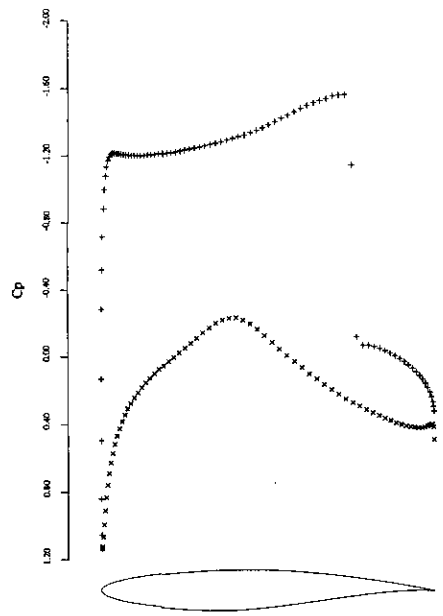

FIG. 17. RAE 2822 with $M = 0.75$, $\alpha = 3.0$, $C_L = 1.1325$, $C_D = 0.0471$.

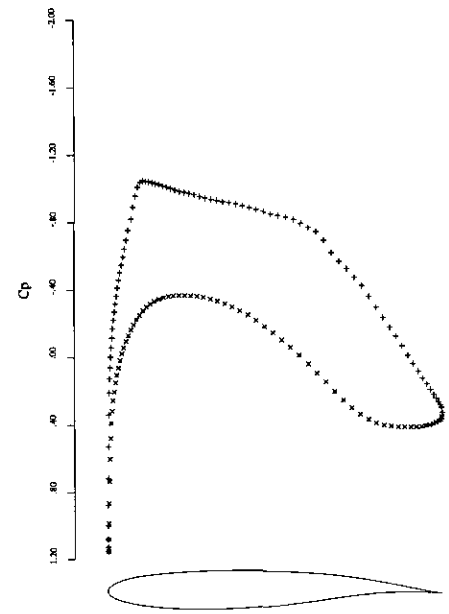

FIG. 19. Korn with $M = 0.75$, $\alpha = 0.0$, $C_L = 0.6321$, $C_D = 0.0002$.

standard high resolution difference schemes [20, 13]. For the NACA0012 airfoil, three different initial conditions of Mach numbers of 0.8, 0.8, and 0.85, with different angles of attack 0.0, 1.25, and 1.0 degrees are used. The mesh and the simulation results after 100 multigrid cycles are presented in Fig. 12, Fig. 13, Fig. 14, and Fig. 15. Similarly, a Mach number 0.75 and angle of attack of 3.0 degrees have been used for the airfoil RAE2822 calculation, and the mesh and result are given in Fig. 16 and Fig. 17. The Korn airfoil is designed for a shock-free transonic solution. The flow distribution around it is very sensitive to the initial Mach number and the numerical algorithms. In our calculation, the designed shock-free condition of Mach number 0.75 and angle of attack of 0.0 degrees are used; the mesh and the output result are shown in Fig. 18 and Fig. 19. All these results show that the steady state scheme captures shocks with two interior points in the discrete shock structure, and provides good accuracy for transonic flows.

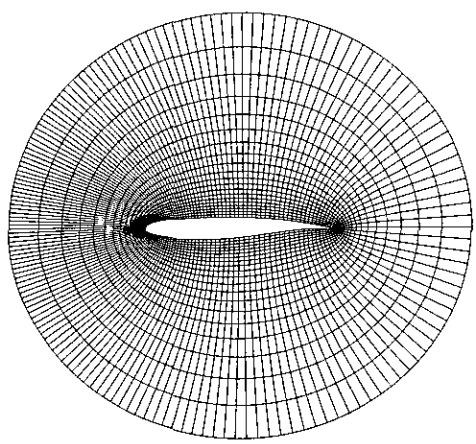

FIG. 18. Mesh for KORN airfoil.

5. CONCLUSION

Blending the collisional gas-kinetic BGK model into the fluxes of a finite volume discretization of the conservation laws offers a promising new approach to the development of numerical hydrodynamics codes. The numerical analysis for the gas-kinetic scheme in this paper provides some physical insight into the flux-vector splitting, Lax–Wendroff schemes, and the role of artificial diffusion. This scheme contains dissipation naturally through the kinetic flux vector splitting in the initial nonequilibrium term f_0. At the same time, the high resolution and multidimensionality of the traditional central difference schemes are recovered from the equilibrium state g. The nonlinear coupling between g and f_0 is modeled on the particle relaxation process, where the collision time τ is directly related to the viscosity coefficient. Also, in this gas-kinetic scheme, the entropy condition is approximately satisfied for the numerical solutions, which precludes the emergence of any unphysical phenomena such as rarefaction shocks. For steady state calculations, a new method has been presented, which combines the fast convergence of the multigrid time stepping method with the favorable shock capturing properties of the gas-kinetic scheme. The numerical analysis and examples in this paper suggests that Boltzmann-type scheme could be very useful in a large number of flow simulations.

ACKNOWLEDGMENTS

We thank J. Shi, S. Lam, and G. Brown for helpful discussions, and P. Roe for reviewing an earlier version of the manuscript. The research in this paper is supported by Grant URI/AFOSR F49620-93-1-0427 for all three authors.

REFERENCES

1. H. Aiso, *Hiroshima Math. J.* **23** (1993).
2. J. B. Bell, P. Colella, and J. A. Trangenstein, *J. Comput. Phys.* **82,** 362 (1989).
3. P. L. Bhatnagar, E. P. Gross and M. Krook, *Phys. Rev.* **94,** 511 (1954).
4. C. Cercignani, *The Boltzmann Equation and its Applications* (Springer-Verlag, New York/Berlin, 1988).
5. C. K. Chu, *Phys. Fluids* **8,** 12 (1965).
6. P. Colella, *J. Comput. Phys.* **87,** 171 (1990).
7. P. Colella and P. Woodward, *J. Comput. Phys.* **54,** 174 (1984).
8. S. M. Deshpande, NASA Langley Tech. Paper No. 2613, 1986 (unpublished).
9. B. Einefldt, C. D. Munz, P. L. Roe, and B. Sjögreen, *J. Comput. Phys.* **92,** 273 (1991).
10. W. Eppard and B. Grossman, "A Multidimensional Kinetic-Based Upwind Solver for the Euler Equations," in *AIAA 11th Computational Fluid Dynamics Conference, Orlando, FL, July, 1993.*
11. A. Harten, *J. Comput. Phys.* **49,** 151 (1983).
12. A. Harten, P. D. Lax, and B. Van Leer, *SIAM Rev.* **25,** 151 (1983).
13. C. Hirsch, *The Numerical Computation of Internal and External Flows* (Wiley, New York, 1990), Vols. 1, 2.
14. A. Jameson, "Numerical Solution of Nonlinear Partial Differential Equations of Mixed Type," in *Numerical Solution of Partial Differential Equations, III, SYNSPADE 1975*, edited by B. Hubbard (Academic Press, New York, 1976).
15. A. Jameson, "Transonic Potential Flow Calculations Using Conservation Form," in *Proceedings, Second AIAA Computational Fluid Dynamics Conference, Hartford, June 1975.*
16. A. Jameson, W. Schmidt, and E. Turkel, AIAA Paper 81-1259, 1981 (unpublished).
17. A Jameson, *Appl. Math. and Comput.* **13,** 327 (1983).
18. A. Jameson, MAE Report No. 1651, Princeton University, March 1984 (unpublished).
19. A. Jameson, "Multigrid Algorithms for Compressible Flow Calculations," in *Proceedings, 2nd European Conference on Multigrid Methods, Cologne, 1985*, edited by W. Hackbusch and U. Trottenberg, Lecture Notes in Mathematics, Vol. 1228 (Springer-Verlag, New York/Berlin, 1986), pp. 166–201.
20. A. Jameson, *Int. J. Numer. Methods Fluids,* **20,** 743, (1995).
21. H. W. Liepmann, R. Narasimha, and M. T. Chahine, *Phys. Fluids* **5,** 1313 (1962).
22. R. W. MacCormack, AIAA Paper 69-354, 1969 (unpublished).
23. R. W. MacCormack and G. V. Candler, *Comput. & Fluids* **17,** No. 1, 135 (1989).
24. M. N. Macrossan, *J. Comput. Phys.* **80,** 204 (1989).
25. M. N. Macrossan and R. I. Oliver, *Int. J. Numer. Methods Fluids* **17,** 177 (1993).
26. J. C. Mandal and S. M. Deshpande, *Comput. & Fluids* **23,** 447 (1994).
27. B. Perthame, *SIAM J. Numer. Anal.* **29,** No. 1 (1992).
28. B. Perthame and E. Tadmor, *Commun. Math. Phys.* **36,** 501 (1991).
29. K. H. Prendergast and K. Xu, *J. Comput. Phys.* **109,** 53 (1993).
30. D. I. Pullin, *J. Comput. Phys.* **34,** 231 (1980).
31. J. Quirk, *Numer. Methods Fluids* **18,** No. 6 (1994).
32. R. D. Reitz, *J. Comput. Phys.* **42,** 108 (1981).
33. R. D. Richtmyer, NCAR Technical Report 63-2, Boulder, CO, 1962 (unpublished).
34. T. W. Roberts, *J. Comput. Phys.* **90,** 141 (1990).
35. P. L. Roe, *Annu. Rev. Fluid Mech.* **18,** 337 (1986).
36. P. L. Roe and D. Sidilkover, *SIAM J. Numer. Anal.* **29,** no. 6, 1542 (1992).
37. R. H. Sanders and K. H. Prendergast, *Astrophys. J.* **188** (1974).
38. C. W. Shu and S. Osher, *J. Comput. Phys.* **77,** 439 (1988).
39. J. L. Steger and R. F. Warming, *J. Comput. Phys.* **40,** 263 (1981).
40. R. C. Swanson and E. Turkel, *J. Comput. Phys.* **101,** 297 (1992).
41. P. K. Sweby, *SIAM J. Numer. Anal.,* **21,** (1984).
42. S. Tatsumi, L. Martinelli, and A. Jameson, *AIAA J.* **33,** No. 2 (1995).
43. P. van Leer, ICASE Report, No. 82-30, September 1982 (unpublished).
44. B. van Leer, J. L. Thomas, P. L. Roe, and R. W. Newsome, AIAA Paper 87-1104, 1987 (unpublished).
45. W. G. Vincenti and C. H. Kruger, *Introduction to Physical Gas Dynamics* (Krieger, Melbourne, FL, 1965).
46. P. Woodward and P. Colella, *J. Comput. Phys.* **54,** 115 (1984).
47. K. Xu and K. H. Prendergast, *J. Comput. Phys.* **114,** 17 (1994).
48. K. Xu, Ph.D. thesis, Columbia University, 1993.